GEOPHYSICAL RESEARCH LETTERS, VOL. 35, L21808, doi:10.1029/2008GL035481, 2008

Extreme changes in stable hydrogen isotopes and precipitation characteristics in a landfalling Pacific storm

Tyler B. Coplen,[1] Paul J. Neiman,[2] Allen B. White,[2] Jurate M. Landwehr,[1]
F. Martin Ralph,[2] and Michael D. Dettinger[3]

Received 25 July 2008; revised 11 September 2008; accepted 30 September 2008; published 13 November 2008.

[1] With a new automated precipitation collector we measured a remarkable decrease of 51‰ in the hydrogen isotope ratio (δ^2H) of precipitation over a 60-minute period during the landfall of an extratropical cyclone along the California coast on 21 March 2005. The rapid drop in δ^2H occurred as precipitation generation transitioned from a shallow to a much deeper cloud layer, in accord with synoptic-scale ascent and deep ''seeder-feeder'' precipitation. Such unexpected δ^2H variations can substantially impact widely used isotope-hydrograph methods. From extreme δ^2H values of −26 and −78‰, we calculate precipitation temperatures of 9.7 and −4.2°C using an adiabatic condensation isotope model, in good agreement with temperatures estimated from surface observations and radar data. This model indicates that 60 percent of the moisture was precipitated during ascent as temperature decreased from 15°C at the ocean surface to −4°C above the measurement site. **Citation:** Coplen, T. B., P. J. Neiman, A. B. White, J. M. Landwehr, F. M. Ralph, and M. D. Dettinger (2008), Extreme changes in stable hydrogen isotopes and precipitation characteristics in a landfalling Pacific storm, *Geophys. Res. Lett.*, *35*, L21808, doi:10.1029/2008GL035481.

1. Introduction

[2] The stable isotopic composition of tropospheric vapor condensation is largely controlled by temperature under adiabatic or pseudo-adiabatic conditions during ascent of air masses, providing a natural tracer of atmospheric processes [*Gedzelman and Lawrence*, 1990; *Scholl et al.*, 2007; *Smith and Evans*, 2007]. Organized ascent can often be found in atmospheric rivers (AR), which are characterized by strong horizontal water-vapor fluxes concentrated in a narrow band in the lower troposphere immediately ahead of polar cold fronts [*Zhu and Newell*, 1998; *Ralph et al.*, 2004]. They are readily identifiable in Special Sensor Microwave/Imager (SSM/I) satellite imagery as long, narrow plumes of enhanced integrated water vapor (IWV) (Figure 1) [*Hollinger et al.*, 1990]. They often produce heavy coastal rainfall and flooding along the U.S. West Coast [*Ralph et al.*, 2006]. During landfalling Pacific winter storms, ARs provide a focused moisture source, leading to orographic rainfall enhancement in the coastal mountains [*Ralph et al.*, 2004; *Bao et al.*, 2006]. These processes have not been studied from simultaneous meteorological and isotopic perspectives because of the difficulty in making both types of measurements concurrently. With stable isotopic results of samples taken with new instrumentation, collocated at a research meteorological site, we report on insights that this combined capability provides in understanding the origin and history of precipitation during a landfalling AR along the northern California coast (Figure 1).

[3] Studies using meteorological arrays have provided insights into precipitation-generating processes [*Neiman et al.*, 2002, 2004; *Kingsmill et al.*, 2006; *Ralph et al.*, 2006] and precipitation characteristics during such storm events [*White et al.*, 2003; *Martner et al.*, 2008]. These meteorological findings helped shape the present work by revealing processes that would be expected to impose distinct isotopic signatures on the resulting precipitation. Notably, precipitation with a radar ''brightband'' (BB) signature falls as the ''seeder'' portion of the ''seeder-feeder'' precipitation mechanism [*Bergeron*, 1965]. (The brightband is a narrow horizontal layer of enhanced radar reflectivity measured in the atmosphere where snow melts to form rain [*Battan*, 1973]. The discrete altitude referred to as BB in this paper is the altitude of the maximum radar reflectivity in the brightband, as measured by the profiling radars used in this study.) Because such precipitation occurs initially at higher (and much colder) altitudes, it would be expected to have an isotopic composition depleted in ^{2}H [*Dansgaard*, 1953]. In contrast, a shallow rainfall process occurring without a BB, i.e., non-brightband (NBB) rain, forms primarily at low altitudes [*White et al.*, 2003] and is expected to exhibit an isotopic composition consistent with a relatively warm marine source. This is the ''feeder'' part of the ''seeder-feeder'' phenomenon.

2. Observing Systems

[4] The California observing couplet used in this study at Bodega Bay (BBY) and Cazadero (CZD) ∼30 km north-northwest of BBY and ∼10 km inland in the coastal mountains at 475 m above mean sea level (MSL) (Figure 1) constitutes an AR observatory, consisting of an unusual combination of vertical radars and specialized meteorological instrumentation.

[5] This study required instrumentation to obtain many time-integrated samples over short (30-min) intervals to capture rapid changes in isotopic composition. An automated precipitation collector (U.S. patent pending) for obtaining 96 sequential 15-mL samples was built (see Figure S1 of the auxiliary material[1]) and installed at CZD. Upon notification

[1]U.S. Geological Survey, Reston, Virginia, USA.
[2]Earth Systems Research Laboratory, NOAA, Boulder, Colorado, USA.
[3]U.S. Geological Survey, Scripps Institution of Oceanography, La Jolla, California, USA.

[1]Auxiliary materials are available in the HTML. doi:10.1029/2008GL035481.

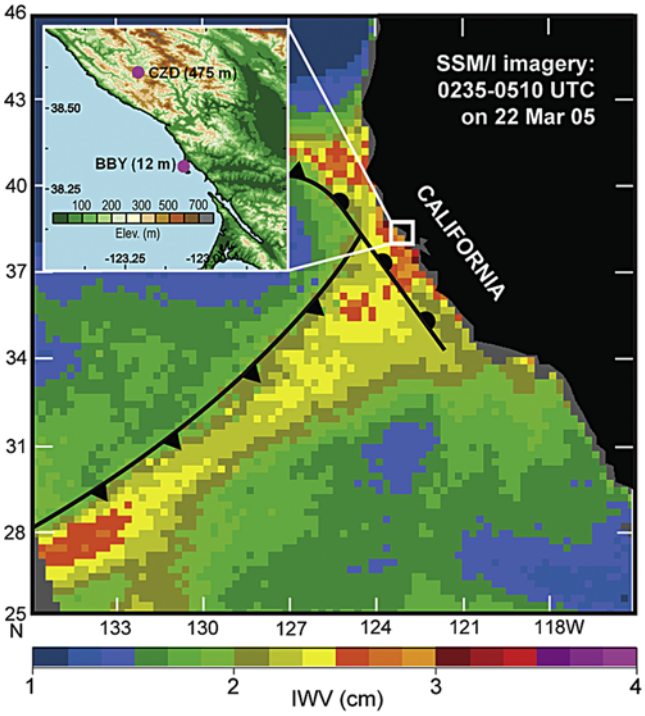

Figure 1. Composite Special Sensor Microwave/Imager satellite image of integrated water vapor (IWV, cm; color bar at bottom) constructed from polar-orbiting swaths between 0235 and 0510 UTC 22 March 2005. Approximate frontal positions are shown at 0300 UTC 22 March. The white box corresponds to the inset terrain base map showing the observing sites at Bodega Bay (BBY) and Cazadero (CZD).

of the approach of the AR by NOAA weather forecasters, the collector was started.

3. Meteorological and Isotopic Chronology

[6] The storm documented here occurred on 21–22 March 2005 when an extratropical cyclone made landfall in California (Figure 1), and then moved steadily eastward, but without exhibiting exceptionally large IWV fluxes. Only modest rainfall (30–40 mm) accumulated in the BBY-CZD region. Figure 2 summarizes observations at BBY of hourly wind profiles and meridional (i.e., southerly-component) isotachs (Figure 2a) and IWV (Figure 2b). Figure 3 summarizes meteorological and isotopic measurements at CZD. S-PROF radar reflectivity profiles of precipitation and clouds [*White et al.*, 2003] allowed an objective differentiation of BB rain from NBB rain (Figures 3a and 3b). Also indicated are NBB periods subjectively determined to have convective rainfall. The δ^2H of precipitation changed distinctly over time (Figure 3d) defining six successive periods, I through VI. The δ^{18}O variations were comparable to those of δ^2H and are not presented here.

[7] At the beginning of period I (1500–2215 UTC 21 March), S-PROF radar reflectivity (Figure 3a) documents the onset of high clouds (~6.5 km MSL) at CZD. By 2000 UTC, these clouds thickened and lowered with the descent of warm-frontal wind shear (stronger winds over weaker winds) that was first observed over BBY at ~4 km MSL (Figure 2a). Such a warm frontal region is often associated with upward vertical motion in the middle to upper troposphere, where clouds and precipitation form aloft. Indeed, IWV (Figure 2b) reveals significant moistening during the warm-frontal descent, with light rain commencing at 2030 UTC. At 2130 UTC, the first surface accumulation occurred at CZD yielding a precipitation δ^2H of −24‰. This was likely generated in part by local shallow orographic forcing [e.g., *Neiman et al.*, 2002]. The mean surface temperature at CZD during period I was ~9.3°C, but temperatures where precipitation formed were likely to be slightly cooler. Also at 2130 UTC, the BBY wind profiler reveals the beginning of a 572-m increase in the BB melting layer, from 1542 m to 2114 m (at 0230 UTC 22 March), in response to warm advection during the warm-frontal descent over the next five hours.

[8] During period II (2215–2315 UTC 21 March), δ^2H values decreased dramatically within 60 min from −25.5 to −77‰, indicating that the precipitation source transitioned rapidly from a predominantly warm (i.e., shallow) region to a much colder one (i.e., more elevated, owing to the deep cloud layer produced by synoptic-scale ascent with the warm front). The delay between the onset of BB rain during

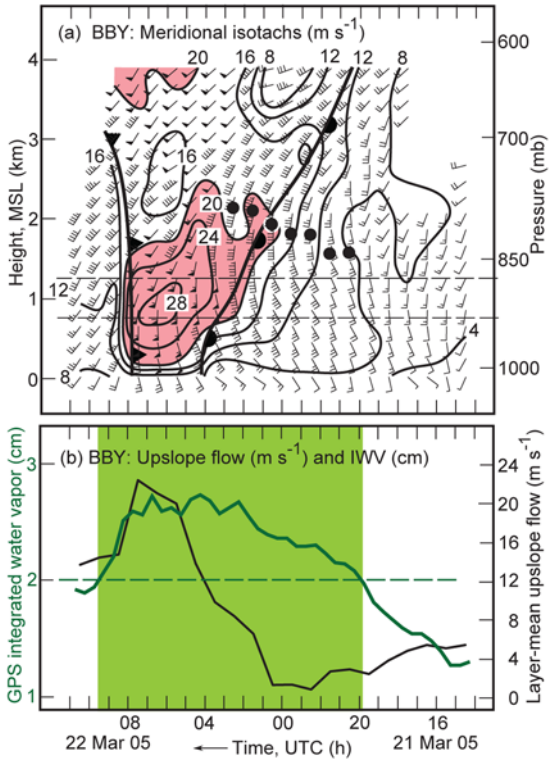

Figure 2. Observations from Bodega Bay, California (BBY) on 21–22 March 2005. Time increases from right to left to portray the advection of fronts from west to east. (a) Time-height section of hourly wind profiles (wind flags = 25 m s^{-1}, barbs = 5 m s^{-1}, half-barbs = 2.5 m s^{-1}), melting levels (black dots), meridional isotachs (m s^{-1}; >20 m s^{-1} red shaded), and fronts. (b) Time-series traces of layer-mean (750–1250 m mean sea level) upslope flow (m s^{-1}; directed from 230°; black) between the dashed lines in Figure 2a, and integrated water vapor (IWV) (cm; green). The green shading marks the position of the atmospheric river, based on IWV >2 cm.

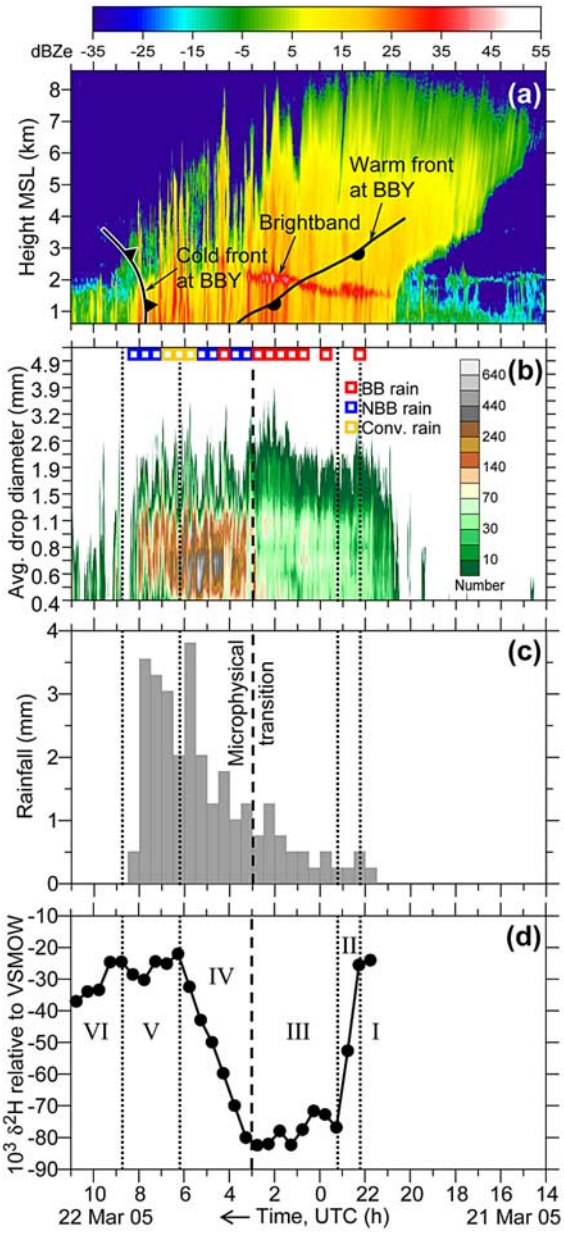

Figure 3. Observations at Cazadero, California (CZD) on 21–22 March 2005. Time increases from right to left. (a) Time-height section of equivalent radar reflectivity factor (dBZe; see color scale). The fronts are as in Figure 2a. (b) Contoured drop-size distributions of rainfall at the surface as a function of time and diameter (see color scale). Open squares indicate objective categorization of the rainfall occurring during each half-hour period (see Text S1 of the auxiliary material). (c) Histogram of hourly rainfall (mm). (d) Time series of stable hydrogen isotopic composition of 30-min, time-integrated precipitation samples. A primary change in precipitation microphysical properties is marked by the vertical dashed lines in Figures 3b–3d. Zones of distinct isotope behavior are enclosed by the vertical lines and labeled with Roman numerals in Figure 3d: I, pre–cold-frontal precipitation of marine air; II, transitional mixing of I and III; III, precipitation from deep, cold cloud layer via the seeder-feeder mechanism; IV, transitional mixing between III and V; V, shallow, locally generated orographic rain; VI, light rainfall with passage of cold front.

period I and the sharp drop in isotopic values that followed is due to the time required for precipitation formed deep in the cloud to fall through the melting layer and reach the surface. The decrease in δ^2H of rain reflects an increasing contribution of cold seeder-cloud precipitation aloft, consistent with the strengthening echoes in the radar BB.

[9] During period III (2315 UTC 21 March to 0300 UTC 22 March), δ^2H varied about a mean value of −78‰ as precipitation continued to be generated by the deep, cold cloud layer via the seeder-feeder mechanism. The effective source region of precipitation was above the BB altitude where seeder precipitation readily forms. Over periods I through III at CZD, BB rain increased in intensity (Figure 3c) while the altitude of the BB ascended during the warm-frontal descent through this layer. At the end of period III (i.e., 0300 UTC) the descending warm front nearly had reached the surface at BBY (Figure 2b).

[10] During period IV (0300–0600 UTC 22 March), δ^2H values increased dramatically from −80 to −22‰, indicating that precipitation was forming at increasingly warmer temperatures. At the beginning of this period, BB precipitation abruptly terminated (Figure 3a), but the precipitation intensified (Figure 3c) as the warm front descended toward the surface, and strong onshore water vapor fluxes, which favor orographic rain enhancement, enveloped the region. After 0315 UTC, there was a marked change in the drop-size distribution toward a preponderance of small drops, consistent with the transition from deep, synoptically forced precipitation to much shallower, locally generated orographic precipitation (Figure 3b). At 0410 UTC, warm-frontal wind shear descended to the surface at BBY, followed by a 28 m s^{-1} south-southwesterly low-level jet centered at ∼1 km MSL in the cyclone warm sector (Figure 2a).

[11] During period V (0615–0845 UTC 22 March), the mean δ^2H value was −26‰ with little variation as locally generated orographic rain continued. Some of the most intense rain rates occurred during this period due to a spike in the upslope flow in combination with enhanced water vapor content (i.e., the low-level water vapor flux was maximized in the pre–cold-frontal low-level jet) (Figure 2b). NBB rain (including embedded convection) persisted until shortly after the cold-frontal passage at ∼0800 UTC 22 March. Although the surface temperature at CZD over period V increased from ∼9.5°C to 11°C, temperatures where precipitation formed were likely cooler than the surface, but much warmer than during the bulk of period IV. Rainfall at CZD diminished at ∼0800 UTC, when observations at BBY revealed an abrupt wind shift from strong southerly to weaker southwesterly below 1 km MSL and a sharp drop in IWV that marked the leading edge of a deep tropospheric cold-frontal passage (Figure 2a).

[12] During period VI (0845–1045 UTC 22 March), δ^2H values decreased as cold air filtered in behind the cold front. The extremely low intensity rainfall that occurred during this period was sampled by the disdrometer and the sequential collector, but not by the tipping-bucket rain gauge (Figures 3b–3d).

4. Synthesis and Discussion

[13] We modeled the δ^2H of CZD precipitation (data available[1]) using the numerical closed-system *Rayleigh*

Table 1. Comparison of *Gonfiantini and Gherardi* [2006] Isotope Model Precipitation Temperatures With Measured or Estimated Precipitation Temperatures at Cazadero, CA

Site	Model Input δ^2H of Precipitation[a]	Model Output		Measured Values t	Comments
		Mole Fraction Precipitated Water	t		
Pacific Ocean	−11.6 ‰	0	15.0°C	∼15.0°C[b]	Initial model parameters, relative humidity 100 percent
CZD	−24.7 ‰	0.19	10.1°C	9°C	Period I, NBB rain; temperature estimated from surface data
CZD	−78 ‰	0.60	−4.2°C	<0°C	Period III, BB precipitation
CZD	−26 ‰	0.20	9.7°C	10°C	Period V, NBB rain; temperature estimated from surface data

[a]Pt-equilibration measurements [*Coplen et al.*, 1991] of δ^2H are expressed relative to VSMOW that is normalized to a δ^2H of SLAP of −428 ‰; 1-σ uncertainty is 1 ‰.

[b]Pacific sea surface temperature off California on 20 March 2005 was ∼15.0°C. See http://weather.unisys.com/archive/sst/sst-050321.gif.

[1896]-based model of *Gonfiantini and Gherardi* [2006], which produces rain by atmospheric vapor condensation under (pseudo)-adiabatic conditions during air-mass ascent. The initial temperature (15.0°C) and δ^2H of rain (−11.6‰; δ^2H of vapor is −94.2‰) forming from saturated Pacific Ocean air (relative humidity 100 percent) used for each run are given in Table 1. We use δ^2H of rain (second column) as an input parameter to calculate precipitation temperature (fourth column) and compare it with precipitation temperature estimated from meteorological data (fifth column). An additional model output is the fraction of precipitated water or rainout (third column). For example, the temperature of the precipitation source region predicted at CZD in period III for δ^2H of −78‰ is −4.2°C, consistent with S-PROF radar observations of a BB that indicate temperatures colder than 0°C where the precipitation forms. The δ^2H values provide an independent confirmation of the seeder-feeder process. For each of the 3 model runs, the discrete temperatures predicted and estimated precipitation temperature ranges show good agreement, despite the wide range in temperature of the precipitation source region. The model also indicates that during period III, 60 percent of air-mass moisture precipitated from the air mass from when its precipitation temperature was 15°C in the Pacific Ocean; but, for period V, the loss from shallower, locally generated orographic precipitation was only 20 percent of moisture despite a higher rainfall rate (Figure 3c). The δ^2H behavior in periods I through IV is similar to the pioneering measurements of *Dansgaard* [1953] who quantified the relation between δ^{18}O and precipitation formation temperatures for a similar mid-latitude coastal storm in Europe more than half a century ago, although he had none of the remote sensing tools and high-frequency sampling capability of this study.

[14] With a new collector, we captured extreme δ^2H variations associated with rapid changes in microphysical processes within a landfalling Pacific storm. Variations of 50‰ in δ^2H of precipitation within 1 h have not been reported before and should substantially inform isotope-hydrograph studies. The dynamics of δ^2H variation are completely missed when only a cumulative, volume-weighted average of δ^2H is determined. The δ^2H in precipitation ranged from ∼−22 to −82‰, yet a composite sample would yield a δ^2H value of ∼−54‰. The seeder-transition signature would have been missed without sequential 30-min sampling and potentially misinterpreted without the meteorological array. In summary, the combination of high resolution isotopic data and multivariate data from meteorological arrays provides an enhanced understanding of the transitions between meteorological regimes.

[15] **Acknowledgments.** The support of the U.S. Geological Survey National Research Program made this report possible. We thank R. Gonfiantini and F. Gherardi for sharing their isotopic numerical model and Scripps Institution of Oceanography for hosting meetings. We are grateful for reviews by I. Winograd, M. Scholl, D. Kingsmill, and J. Miller. We commend the talented engineering staff at NOAA/ESRL/PSD for operating the AR observatory.

References

Bao, J.-W., S. A. Michelson, P. J. Neiman, F. M. Ralph, and J. M. Wilczak (2006), Interpretation of enhanced integrated water-vapor bands associated with extratropical cyclones: Their formation and connection to tropical moisture, *Mon. Weather Rev.*, *134*, 1063–1080.

Battan, L. J. (1973), *Radar Observations of the Atmosphere*, 324 pp., Univ. of Chicago Press, Chicago, Ill.

Bergeron, T. (1965), On the low-level redistribution of atmospheric water caused by orography, paper presented at the International Conference on Cloud Physics, Int. Assoc. of Meteorol. and Atmos. Phys., Tokyo.

Coplen, T. B., J. D. Wildman, and J. Chen (1991), Improvements in the gaseous hydrogen-water equilibration technique for hydrogen isotope ratio analysis, *Anal. Chem.*, *63*, 910–912.

Dansgaard, W. (1953), The abundance of O^{18} in atmospheric water and water vapour, *Tellus*, *5*, 461–469.

Gedzelman, S. D., and J. R. Lawrence (1990), The isotopic composition of precipitation from two extratropical cyclones, *Mon. Weather Rev.*, *118*, 495–509.

Gonfiantini, R., and F. Gherardi (2006), Modelling the isotopic composition of precipitation, in *International Workshop on Isotopic Effects in Evaporation, Revisiting the Craig-Gordon Model Four Decades After Its Formulation*, pp. 86–89, Cons. Naz. delle Ric., Pisa, Italy.

Hollinger, J. P., J. L. Peirce, and G. A. Poe (1990), SSM/I instrument evaluation, *IEEE Trans. Geosci. Remote Sens.*, *28*, 781–790.

Kingsmill, D. E., P. J. Neiman, F. M. Ralph, and A. B. White (2006), Synoptic and topographic variability of northern California precipitation characteristics in landfalling winter storms observed during CALJET, *Mon. Weather Rev.*, *134*, 2072–2094.

Martner, B. E., S. E. Yuter, A. B. White, S. Y. Matrosov, D. E. Kingsmill, and F. M. Ralph (2008), Raindrop size distributions and rain characteristics in California coastal rainfall for periods with and without a radar brightband, *J. Hydrometeorol.*, *8*, 154–166.

Neiman, P. J., F. M. Ralph, A. B. White, D. E. Kingsmill, and P. O. G. Persson (2002), The statistical relationship between upslope flow and rainfall in California's coastal mountains: Observations during CALJET, *Mon. Weather Rev.*, *130*, 1468–1492.

Neiman, P. J., P. O. G. Persson, F. M. Ralph, D. P. Jorgensen, A. B. White, and D. E. Kingsmill (2004), Modification of fronts and precipitation by coastal blocking during an intense landfalling winter storm in southern California: Observations during CALJET, *Mon. Weather Rev.*, *132*, 242–273.

Ralph, F. M., P. J. Neiman, and G. A. Wick (2004), Satellite and CALJET aircraft observations of atmospheric rivers over the eastern North Pacific Ocean during the winter of 1997/98, *Mon. Weather Rev.*, *132*, 1721–1745.

Ralph, F. M., P. J. Neiman, G. A. Wick, S. I. Gutman, M. D. Dettinger, D. R. Cayan, and A. B. White (2006), Flooding on California's Russian River: Role of atmospheric rivers, *Geophys. Res. Lett.*, *33*, L13801, doi:10.1029/2006GL026689.

Rayleigh (1896), Theoretical considerations respecting the separation of gases by diffusion and similar processes, *Philos. Mag.*, *42*, 493–498.

Scholl, M. A., T. W. Giambelluca, S. B. Gingerich, M. A. Nullet, and L. L. Loope (2007), Cloud water in windward and leeward mountain forests: The stable isotope signature of orographic cloud water, *Water Resour. Res.*, *43*, W12411, doi:10.1029/2007WR006011.

Smith, R. B., and J. P. Evans (2007), Orographic precipitation and water vapor fractionation over the southern Andes, *J. Hydrometeorol.*, *8*, 3–19.

White, A. B., P. J. Neiman, F. M. Ralph, D. E. Kingsmill, and P. O. G. Persson (2003), Coastal orographic rainfall processes observed by radar during the California Land-falling Jets Experiment, *J. Hydrometeorol.*, *4*, 264–282.

Zhu, Y., and R. Newell (1998), A proposed algorithm for moisture fluxes from atmospheric rivers, *Mon. Weather Rev.*, *126*, 725–735.

T. B. Coplen and J. M. Landwehr, U.S. Geological Survey, 431 National Center, Reston, VA 22092, USA. (tbcoplen@usgs.gov)

M. D. Dettinger, U.S. Geological Survey, Scripps Institution of Oceanography, Room 0224, La Jolla, CA 92093, USA.

P. J. Neiman, F. M. Ralph, and A. B. White, Earth Systems Research Laboratory, NOAA, 325 Broadway, Boulder, CO 80305, USA.

Auxiliary Material

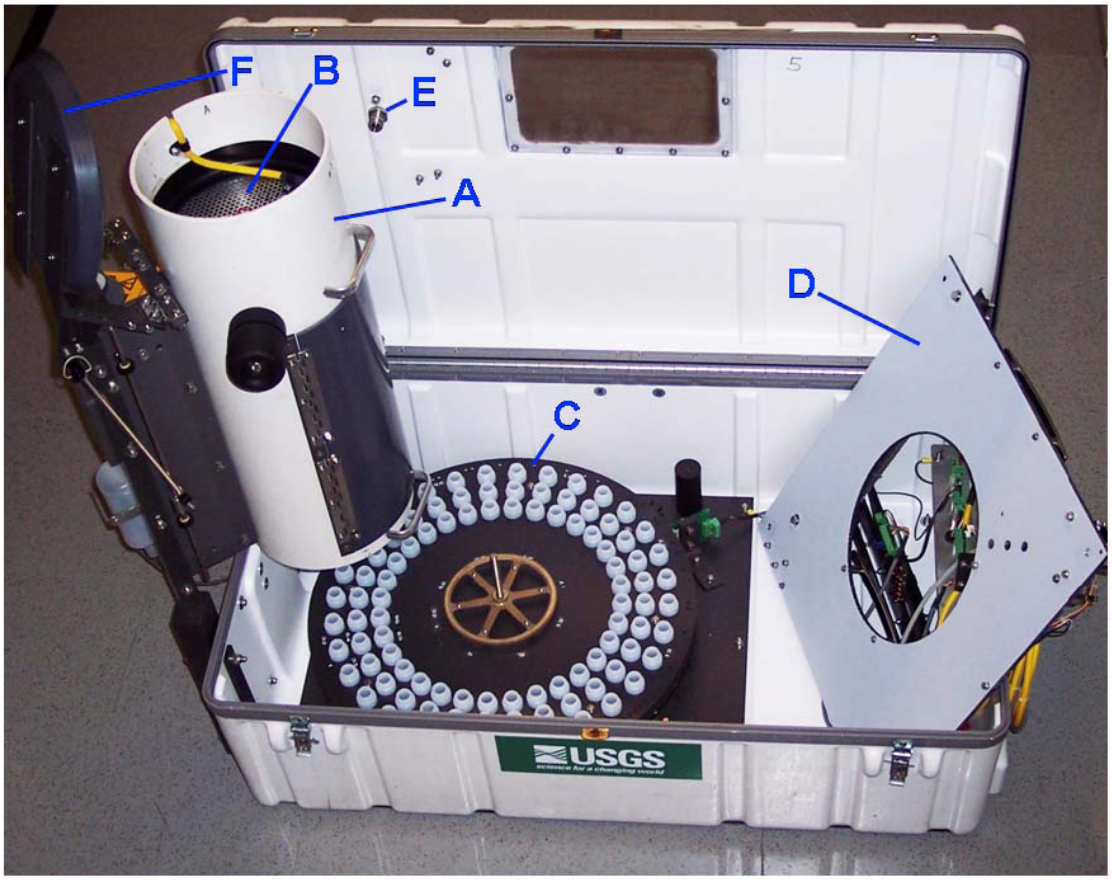

Figure S1. Sequential, time-integrating precipitation collector. A: 25-cm-diameter funnel with an electrically actuated valve collects continuously over the course of an event at 30-min (or other selected) intervals until an electrically actuated valve is opened to allow the time-integrated precipitation sample to flow by gravity into a 15-mL funnel. Water in excess of 15 mL spills over the lower funnel and flows to the ground. Subsequently, an electrically actuated valve on the 15-mL funnel is opened and this aliquot is delivered by transfer tubing through entrance E into a clean vial]. B: Heated funnel top—melts hail and snow. C: 96 20-mL vials (having a volume selected to minimize isotopic fractionation of precipitation samples that can occur in collectors having sample volumes with large headspace, such as 500 mL or more) in motor-driven carousel that uses infrared detectors for positioning. D: Teflon-coated vial cover minimizes evaporation and subsequent isotopic fractionation. E: Orifice for transfer of sample between funnel (A) assembly and vial in carousel. F: Linear-actuator-driven lid of funnel assembly.

Auxiliary Material Text S1

The Atmospheric River Observatory

The Atmospheric River Observatory consists of the unusual combination of vertical radars and specialized instrumentation needed to monitor continuously coastal and orographic rainfall processes, as well as the atmospheric river conditions that enhance the precipitation. The meteorological instruments in the atmospheric river observatory were distributed between two sites. The coastal site at Bodega Bay (BBY) [12 m mean sea level (MSL)] featured an all-weather 915-MHz wind profiler and a global positioning system (GPS) receiver. The wind profiler measured hourly averaged vertical profiles of the horizontal wind with 100-m vertical resolution from 100 m to ~4 km above ground, with 1 m s-1 wind-speed accuracy [Carter et al., 1995]. The wind profiler also monitored the altitude of the radar brightband (BB) on an hourly basis when precipitation was falling [White et al., 2002]. Collocated observations of vertically integrated water vapor (IWV) were obtained every 30 min from the GPS receiver with ~1-mm accuracy [Wolfe and Gutman, 2000]. Concurrent precipitation observations were obtained at Cazadero (CZD), located in the coastal mountains 30 km north-northwest of BBY. An S-band (lambda = 10 cm) precipitation profiler (S-PROF) [White et al., 2003] provided vertical profiles of the equivalent radar reflectivity factor and vertical radial velocity every 41 s from 142 m to ~8 km above ground. The S-PROF observations characterized the bulk microphysical properties of the precipitation using the automated rainfall process partitioning algorithm developed by White et al. [2002]. In particular, the algorithm objectively distinguishes rainfall occurring with a brightband (BB rain) from rainfall occurring without a brightband (NBB rain). A portion of the NBB rain was subjectively classified as being convective in nature. A companion Joss-Waldvogel disdrometer [Joss and Waldvogel, 1967] counted and measured the sizes of the raindrops reaching the surface by sensing the vertical momentum of drops impacting on its 50-cm² exposed surface. Drops were automatically counted in 20 size categories ranging from approximately 0.35 to 5.4 mm in diameter, and the raw data counts were accumulated and recorded in one-minute intervals. At each site, a tipping-bucket rain gauge measured rainfall with ~0.25-mm resolution and a 10-m tower provided pressure, temperature, humidity, radiative fluxes, and vector wind, all with 2-min sampling. Finally, IWV over the oceans was mapped for the study period by three polar-orbiting satellites, each with a special sensor microwave/imager (SSM/I) [Hollinger et al., 1990].

Automated precipitation collector

To obtain many time-integrated samples over short (30-min) intervals to capture rapid changes in isotopic composition, a new automated precipitation collector (U.S. patent pending) for obtaining 96 sequential 15-mL samples was designed, built, and installed at CZD (Figure S1). This collector is contrasted with the 5-sample arid-zone collector optimized for 1-month storage periods [Adar et al., 1980] and a 20-sample sequential volume-integrating collector [Adar et al., 1991]. Although sequential precipitation studies with intervals from minutes to hours have been conducted by Rindsberger et al. [1991] and Celle-Jeanton et al. [2004], this study collected samples in the presence of an

extended meteorological observation array that characterized precipitation-formation conditions.

The Gonfiantini and Gheradi [2006] Model

Gonfiantini and Gheradi [2006] modeled the isotopic composition of precipitation both with air-mass cooling by adiabatic expansion and by isobaric conditions. Their model employs Rayleigh-type equations for isotope mass balance calculations to determine the isotopic composition of precipitation as a function of the formation temperature of precipitation at intervals of 0.05 degree. The model assumes that vapor condensation takes place at isotopic equilibrium and it requires the equilibrium isotopic fractionation between liquid water and water vapor as a function of temperature; it uses those values published by Majoube [1971]. The model parameters used here assume that rain, once formed in a cloud, is removed from the system by precipitation with no subsequent exchange. Although the model can accommodate precipitation of snow, we did not utilize this feature because precipitation of super-cooled water is expected at temperatures between 0 and –5 degrees C.

References

Adar, E. M., A. Karnieli, B. Z. Sandler, A. S. Issar, M. Wolf, and L. Landsman (1991), A mechanical sequential rain sampler for isotopic and chemical analyses, Rep. 5542/RO/RB, Int. Atom. Energ. Agency.

Adar, E., M. Levin, and A. Barzilai (1980), Development of a self-sealing rain sampler for arid zones, Water Resour. Res., 16, 592–596.

Carter, D. A., K. S. Gage, W. L. Ecklund, W. M. Angevine, P.E. Johnston, A. C. Riddle, J. S. Wilson, and C. R. Williams (1995), Developments in UHF lower tropospheric wind profiling at NOAA's Aeronomy Laboratory, Radio Sci., 30, 997-1001.

Celle-Jeanton, H., R. Gonfiantini, Y. Travi, and B. Sol (2004), Oxygen-18 variations of rainwater during precipitation: Application of the Rayleigh model to selected rainfalls in Southern France, J. Hydrol., 289, 165–177.

Gonfiantini, R., and F. Gherardi (2006), Modelling the isotopic composition of precipitation, in International Workshop on Isotopic Effects in Evaporation, Revisiting the Craig-Gordon Model Four Decades after its Formulation, pp. 86-89, Consiglio Nazionale delle Ricerche, Pisa, Italy.

Hollinger, J. P., J. L. Peirce, and G. A. Poe (1990), SSM/I instrument evaluation, IEEE Trans. Geosci. Remote Sens., 28, 781-790.

Joss, J., and A. Waldvogel (1967), Ein spectrograph für niederschlagstrophen mit automatischer auswertung, Pure Appl. Geophys., 68, 240-246.

Majoube, M. (1971), Fractionnement en oxygène-18 et en deutérium entre l'eau et sa vapeur, J. Chim. Phys., 69, 1423-1436.

Rindsberger, M., S. Jaffe, S. Rahamim, and J. R. Gat (1990), Patterns of the isotopic composition of precipitation in time and space: Data from the Israeli storm water collection program, Tellus, Ser. B, 42, 263–271.

White, A. B., D. J. Gottas, E. Strem, F. M. Ralph, and P. J. Neiman (2002), An automated bright-band height detection algorithm for use with Doppler radar vertical spectral moments, J. Oceanic Atmos. Technol., 19, 687-697.

White, A. B., P. J. Neiman, F. M. Ralph, D. E. Kingsmill, P. O. G. Persson (2003), Coastal orographic rainfall processes observed by radar during the California Land-falling Jets Experiment, J. Hydrometeor., 4, 264-282.

Wolfe, D. E., and S. I. Gutman (2000), Developing an operational, surface-based, GPS, water-vapor observing system for NOAA: Network design and results, J. Atmos. Oceanic Technol., 17, 426-440.

Table S1

Stable hydrogen isotopic composition of precipitation measured in this study.

time-date	d2H
21:30 UTC March 21, 2005	-24
22:00 UTC March 21, 2005	-25.5
22:30 UTC March 21, 2005	-52.6
23:00 UTC March 21, 2005	-76.8
23:30 UTC March 21, 2005	-72.7
00:00 UTC March 22, 2005	-71.6
00:30 UTC March 22, 2005	-77.5
01:00 UTC March 22, 2005	-82.3
01:30 UTC March 22, 2005	-77.9
02:00 UTC March 22, 2005	-82
02:30 UTC March 22, 2005	-82.4
03:00 UTC March 22, 2005	-80
03:30 UTC March 22, 2005	-69.9
04:00 UTC March 22, 2005	-59.7
04:30 UTC March 22, 2005	-49.9
05:00 UTC March 22, 2005	-42.9
05:30 UTC March 22, 2005	-32.4
06:00 UTC March 22, 2005	-22
06:30 UTC March 22, 2005	-25.1
07:00 UTC March 22, 2005	-24.4
07:30 UTC March 22, 2005	-30.2
08:00 UTC March 22, 2005	-28.5
08:30 UTC March 22, 2005	-24.5
09:00 UTC March 22, 2005	-24.6
09:30 UTC March 22, 2005	-33.4
10:00 UTC March 22, 2005	-33.9
10:30 UTC March 22, 2005	-37

Table S2

Gonfiantini and Gheradi [2006] model data of stable hydrogen isotopic composition of precipitation and air-mass vapor during adiabatic condensation.

t	alpha	1-f	d2H-liq	d2H-vap
15	1.09113	0.00	-11.62	-94.17
14.95	1.09119	0.00	-11.74	-94.33
14.9	1.09126	0.01	-11.86	-94.50
14.85	1.09132	0.01	-11.99	-94.66
14.8	1.09138	0.01	-12.11	-94.83
14.75	1.09145	0.01	-12.23	-94.99
14.7	1.09151	0.01	-12.36	-95.16
14.65	1.09157	0.02	-12.48	-95.33
14.6	1.09164	0.02	-12.61	-95.49
14.55	1.09170	0.02	-12.73	-95.66
14.5	1.09176	0.02	-12.86	-95.83
14.45	1.09183	0.02	-12.98	-96.00
14.4	1.09189	0.03	-13.11	-96.16
14.35	1.09196	0.03	-13.23	-96.33
14.3	1.09202	0.03	-13.36	-96.50
14.25	1.09208	0.03	-13.49	-96.67
14.2	1.09215	0.03	-13.61	-96.84
14.15	1.09221	0.04	-13.74	-97.01
14.1	1.09227	0.04	-13.87	-97.17
14.05	1.09234	0.04	-13.99	-97.34
14	1.09240	0.04	-14.12	-97.51
13.95	1.09247	0.04	-14.25	-97.68
13.9	1.09253	0.05	-14.38	-97.85
13.85	1.09260	0.05	-14.50	-98.02
13.8	1.09266	0.05	-14.63	-98.19
13.75	1.09272	0.05	-14.76	-98.36
13.7	1.09279	0.05	-14.89	-98.53
13.65	1.09285	0.06	-15.02	-98.71
13.6	1.09292	0.06	-15.15	-98.88
13.55	1.09298	0.06	-15.28	-99.05
13.5	1.09305	0.06	-15.41	-99.22
13.45	1.09311	0.06	-15.54	-99.39
13.4	1.09318	0.06	-15.67	-99.57
13.35	1.09324	0.07	-15.80	-99.74
13.3	1.09330	0.07	-15.93	-99.91
13.25	1.09337	0.07	-16.06	-100.08
13.2	1.09343	0.07	-16.19	-100.26
13.15	1.09350	0.07	-16.32	-100.43
13.1	1.09356	0.08	-16.45	-100.60
13.05	1.09363	0.08	-16.58	-100.78
13	1.09369	0.08	-16.72	-100.95
12.95	1.09376	0.08	-16.85	-101.13
12.9	1.09382	0.08	-16.98	-101.30
12.85	1.09389	0.09	-17.11	-101.48
12.8	1.09395	0.09	-17.25	-101.65
12.75	1.09402	0.09	-17.38	-101.83
12.7	1.09409	0.09	-17.51	-102.00
12.65	1.09415	0.09	-17.65	-102.18
12.6	1.09422	0.10	-17.78	-102.35
12.55	1.09428	0.10	-17.91	-102.53
12.5	1.09435	0.10	-18.05	-102.71
12.45	1.09441	0.10	-18.18	-102.88
12.4	1.09448	0.10	-18.32	-103.06
12.35	1.09454	0.10	-18.45	-103.24
12.3	1.09461	0.11	-18.59	-103.41
12.25	1.09468	0.11	-18.72	-103.59
12.2	1.09474	0.11	-18.86	-103.77
12.15	1.09481	0.11	-19.00	-103.95
12.1	1.09487	0.11	-19.13	-104.13
12.05	1.09494	0.12	-19.27	-104.30
12	1.09500	0.12	-19.40	-104.48
11.95	1.09507	0.12	-19.54	-104.66

11.9	1.09514	0.12	-19.68	-104.84
11.85	1.09520	0.12	-19.82	-105.02
11.8	1.09527	0.13	-19.95	-105.20
11.75	1.09534	0.13	-20.09	-105.38
11.7	1.09540	0.13	-20.23	-105.56
11.65	1.09547	0.13	-20.37	-105.74
11.6	1.09553	0.13	-20.51	-105.92
11.55	1.09560	0.13	-20.65	-106.10
11.5	1.09567	0.14	-20.79	-106.28
11.45	1.09573	0.14	-20.92	-106.47
11.4	1.09580	0.14	-21.06	-106.65
11.35	1.09587	0.14	-21.20	-106.83
11.3	1.09593	0.14	-21.34	-107.01
11.25	1.09600	0.15	-21.48	-107.19
11.2	1.09607	0.15	-21.63	-107.38
11.15	1.09613	0.15	-21.77	-107.56
11.1	1.09620	0.15	-21.91	-107.74
11.05	1.09627	0.15	-22.05	-107.93
11	1.09633	0.15	-22.19	-108.11
10.95	1.09640	0.16	-22.33	-108.29
10.9	1.09647	0.16	-22.47	-108.48
10.85	1.09654	0.16	-22.62	-108.66
10.8	1.09660	0.16	-22.76	-108.85
10.75	1.09667	0.16	-22.90	-109.03
10.7	1.09674	0.17	-23.04	-109.22
10.65	1.09680	0.17	-23.19	-109.40
10.6	1.09687	0.17	-23.33	-109.59
10.55	1.09694	0.17	-23.48	-109.77
10.5	1.09701	0.17	-23.62	-109.96
10.45	1.09707	0.17	-23.76	-110.14
10.4	1.09714	0.18	-23.91	-110.33
10.35	1.09721	0.18	-24.05	-110.52
10.3	1.09728	0.18	-24.20	-110.71
10.25	1.09734	0.18	-24.34	-110.89
10.2	1.09741	0.18	-24.49	-111.08
10.15	1.09748	0.18	-24.63	-111.27
10.1	1.09755	0.19	-24.78	-111.46
10.05	1.09761	0.19	-24.93	-111.64
10	1.09768	0.19	-25.07	-111.83
9.95	1.09775	0.19	-25.22	-112.02
9.9	1.09782	0.19	-25.37	-112.21
9.85	1.09789	0.20	-25.51	-112.40
9.8	1.09796	0.20	-25.66	-112.59
9.75	1.09802	0.20	-25.81	-112.78
9.7	1.09809	0.20	-25.96	-112.97
9.65	1.09816	0.20	-26.11	-113.16
9.6	1.09823	0.20	-26.26	-113.35
9.55	1.09830	0.21	-26.40	-113.54
9.5	1.09836	0.21	-26.55	-113.73
9.45	1.09843	0.21	-26.70	-113.92
9.4	1.09850	0.21	-26.85	-114.11
9.35	1.09857	0.21	-27.00	-114.31
9.3	1.09864	0.21	-27.15	-114.50
9.25	1.09871	0.22	-27.30	-114.69
9.2	1.09878	0.22	-27.45	-114.88
9.15	1.09884	0.22	-27.60	-115.07
9.1	1.09891	0.22	-27.76	-115.27
9.05	1.09898	0.22	-27.91	-115.46
9	1.09905	0.22	-28.06	-115.65
8.95	1.09912	0.23	-28.21	-115.85
8.9	1.09919	0.23	-28.36	-116.04
8.85	1.09926	0.23	-28.52	-116.24
8.8	1.09933	0.23	-28.67	-116.43
8.75	1.09940	0.23	-28.82	-116.63
8.7	1.09947	0.24	-28.97	-116.82
8.65	1.09954	0.24	-29.13	-117.02
8.6	1.09960	0.24	-29.28	-117.21
8.55	1.09967	0.24	-29.44	-117.41
8.5	1.09974	0.24	-29.59	-117.60
8.45	1.09981	0.24	-29.74	-117.80

8.4	1.09988	0.25	-29.90	-118.00
8.35	1.09995	0.25	-30.05	-118.19
8.3	1.10002	0.25	-30.21	-118.39
8.25	1.10009	0.25	-30.37	-118.59
8.2	1.10016	0.25	-30.52	-118.78
8.15	1.10023	0.25	-30.68	-118.98
8.1	1.10030	0.26	-30.83	-119.18
8.05	1.10037	0.26	-30.99	-119.38
8	1.10044	0.26	-31.15	-119.58
7.95	1.10051	0.26	-31.30	-119.78
7.9	1.10058	0.26	-31.46	-119.97
7.85	1.10065	0.26	-31.62	-120.17
7.8	1.10072	0.27	-31.78	-120.37
7.75	1.10079	0.27	-31.94	-120.57
7.7	1.10086	0.27	-32.09	-120.77
7.65	1.10093	0.27	-32.25	-120.97
7.6	1.10100	0.27	-32.41	-121.17
7.55	1.10107	0.27	-32.57	-121.38
7.5	1.10114	0.28	-32.73	-121.58
7.45	1.10121	0.28	-32.89	-121.78
7.4	1.10128	0.28	-33.05	-121.98
7.35	1.10135	0.28	-33.21	-122.18
7.3	1.10142	0.28	-33.37	-122.38
7.25	1.10150	0.28	-33.53	-122.59
7.2	1.10157	0.29	-33.69	-122.79
7.15	1.10164	0.29	-33.86	-122.99
7.1	1.10171	0.29	-34.02	-123.19
7.05	1.10178	0.29	-34.18	-123.40
7	1.10185	0.29	-34.34	-123.60
6.95	1.10192	0.29	-34.50	-123.81
6.9	1.10199	0.29	-34.67	-124.01
6.85	1.10206	0.30	-34.83	-124.21
6.8	1.10213	0.30	-34.99	-124.42
6.75	1.10220	0.30	-35.16	-124.62
6.7	1.10228	0.30	-35.32	-124.83
6.65	1.10235	0.30	-35.49	-125.04
6.6	1.10242	0.30	-35.65	-125.24
6.55	1.10249	0.31	-35.81	-125.45
6.5	1.10256	0.31	-35.98	-125.65
6.45	1.10263	0.31	-36.14	-125.86
6.4	1.10270	0.31	-36.31	-126.07
6.35	1.10278	0.31	-36.48	-126.27
6.3	1.10285	0.31	-36.64	-126.48
6.25	1.10292	0.32	-36.81	-126.69
6.2	1.10299	0.32	-36.98	-126.90
6.15	1.10306	0.32	-37.14	-127.11
6.1	1.10314	0.32	-37.31	-127.31
6.05	1.10321	0.32	-37.48	-127.52
6	1.10328	0.32	-37.64	-127.73
5.95	1.10335	0.33	-37.81	-127.94
5.9	1.10342	0.33	-37.98	-128.15
5.85	1.10350	0.33	-38.15	-128.36
5.8	1.10357	0.33	-38.32	-128.57
5.75	1.10364	0.33	-38.49	-128.78
5.7	1.10371	0.33	-38.66	-128.99
5.65	1.10378	0.33	-38.83	-129.20
5.6	1.10386	0.34	-39.00	-129.41
5.55	1.10393	0.34	-39.17	-129.63
5.5	1.10400	0.34	-39.34	-129.84
5.45	1.10407	0.34	-39.51	-130.05
5.4	1.10415	0.34	-39.68	-130.26
5.35	1.10422	0.34	-39.85	-130.47
5.3	1.10429	0.35	-40.02	-130.69
5.25	1.10437	0.35	-40.19	-130.90
5.2	1.10444	0.35	-40.37	-131.11
5.15	1.10451	0.35	-40.54	-131.33
5.1	1.10458	0.35	-40.71	-131.54
5.05	1.10466	0.35	-40.89	-131.75
5	1.10473	0.35	-41.06	-131.97
4.95	1.10480	0.36	-41.23	-132.18

4.9	1.10488	0.36	-41.41	-132.40
4.85	1.10495	0.36	-41.58	-132.61
4.8	1.10502	0.36	-41.76	-132.83
4.75	1.10510	0.36	-41.93	-133.04
4.7	1.10517	0.36	-42.11	-133.26
4.65	1.10524	0.37	-42.28	-133.48
4.6	1.10532	0.37	-42.46	-133.69
4.55	1.10539	0.37	-42.63	-133.91
4.5	1.10546	0.37	-42.81	-134.13
4.45	1.10554	0.37	-42.98	-134.34
4.4	1.10561	0.37	-43.16	-134.56
4.35	1.10569	0.37	-43.34	-134.78
4.3	1.10576	0.38	-43.52	-135.00
4.25	1.10583	0.38	-43.69	-135.22
4.2	1.10591	0.38	-43.87	-135.44
4.15	1.10598	0.38	-44.05	-135.65
4.1	1.10606	0.38	-44.23	-135.87
4.05	1.10613	0.38	-44.41	-136.09
4	1.10620	0.38	-44.59	-136.31
3.95	1.10628	0.39	-44.77	-136.53
3.9	1.10635	0.39	-44.95	-136.75
3.85	1.10643	0.39	-45.13	-136.97
3.8	1.10650	0.39	-45.31	-137.20
3.75	1.10658	0.39	-45.49	-137.42
3.7	1.10665	0.39	-45.67	-137.64
3.65	1.10672	0.39	-45.85	-137.86
3.6	1.10680	0.40	-46.03	-138.08
3.55	1.10687	0.40	-46.21	-138.30
3.5	1.10695	0.40	-46.39	-138.53
3.45	1.10702	0.40	-46.58	-138.75
3.4	1.10710	0.40	-46.76	-138.97
3.35	1.10717	0.40	-46.94	-139.20
3.3	1.10725	0.40	-47.12	-139.42
3.25	1.10732	0.41	-47.31	-139.64
3.2	1.10740	0.41	-47.49	-139.87
3.15	1.10747	0.41	-47.68	-140.09
3.1	1.10755	0.41	-47.86	-140.32
3.05	1.10762	0.41	-48.04	-140.54
3	1.10770	0.41	-48.23	-140.77
2.95	1.10777	0.41	-48.41	-140.99
2.9	1.10785	0.42	-48.60	-141.22
2.85	1.10792	0.42	-48.79	-141.45
2.8	1.10800	0.42	-48.97	-141.67
2.75	1.10808	0.42	-49.16	-141.90
2.7	1.10815	0.42	-49.35	-142.13
2.65	1.10823	0.42	-49.53	-142.35
2.6	1.10830	0.42	-49.72	-142.58
2.55	1.10838	0.43	-49.91	-142.81
2.5	1.10845	0.43	-50.10	-143.04
2.45	1.10853	0.43	-50.28	-143.27
2.4	1.10861	0.43	-50.47	-143.49
2.35	1.10868	0.43	-50.66	-143.72
2.3	1.10876	0.43	-50.85	-143.95
2.25	1.10883	0.43	-51.04	-144.18
2.2	1.10891	0.44	-51.23	-144.41
2.15	1.10899	0.44	-51.42	-144.64
2.1	1.10906	0.44	-51.61	-144.87
2.05	1.10914	0.44	-51.80	-145.10
2	1.10922	0.44	-51.99	-145.33
1.95	1.10929	0.44	-52.18	-145.56
1.9	1.10937	0.44	-52.37	-145.80
1.85	1.10945	0.45	-52.56	-146.03
1.8	1.10952	0.45	-52.76	-146.26
1.75	1.10960	0.45	-52.95	-146.49
1.7	1.10968	0.45	-53.14	-146.73
1.65	1.10975	0.45	-53.34	-146.96
1.6	1.10983	0.45	-53.53	-147.19
1.55	1.10991	0.45	-53.72	-147.43
1.5	1.10998	0.46	-53.92	-147.66
1.45	1.11006	0.46	-54.11	-147.89

1.4	1.11014	0.46	-54.30	-148.13
1.35	1.11021	0.46	-54.50	-148.36
1.3	1.11029	0.46	-54.69	-148.60
1.25	1.11037	0.46	-54.89	-148.83
1.2	1.11045	0.46	-55.09	-149.07
1.15	1.11052	0.46	-55.28	-149.30
1.1	1.11060	0.47	-55.48	-149.54
1.05	1.11068	0.47	-55.67	-149.78
1	1.11076	0.47	-55.87	-150.01
0.95	1.11083	0.47	-56.07	-150.25
0.9	1.11091	0.47	-56.27	-150.49
0.85	1.11099	0.47	-56.46	-150.72
0.8	1.11107	0.47	-56.66	-150.96
0.75	1.11114	0.48	-56.86	-151.20
0.7	1.11122	0.48	-57.06	-151.44
0.65	1.11130	0.48	-57.26	-151.68
0.6	1.11138	0.48	-57.46	-151.92
0.55	1.11146	0.48	-57.66	-152.16
0.5	1.11153	0.48	-57.86	-152.39
0.45	1.11161	0.48	-58.06	-152.63
0.4	1.11169	0.48	-58.26	-152.87
0.35	1.11177	0.49	-58.46	-153.12
0.3	1.11185	0.49	-58.66	-153.36
0.25	1.11193	0.49	-58.86	-153.60
0.2	1.11200	0.49	-59.06	-153.84
0.15	1.11208	0.49	-59.27	-154.08
0.1	1.11216	0.49	-59.47	-154.32
0.05	1.11224	0.49	-59.67	-154.56
0.0	1.11232	0.50	-59.87	-154.81
-0.05	1.11240	0.50	-60.08	-155.05
-0.1	1.11248	0.50	-60.28	-155.29
-0.15	1.11256	0.50	-60.49	-155.53
-0.2	1.11263	0.50	-60.69	-155.78
-0.25	1.11271	0.50	-60.89	-156.02
-0.3	1.11279	0.50	-61.10	-156.27
-0.35	1.11287	0.50	-61.30	-156.51
-0.4	1.11295	0.51	-61.51	-156.76
-0.45	1.11303	0.51	-61.72	-157.00
-0.5	1.11311	0.51	-61.92	-157.25
-0.55	1.11319	0.51	-62.13	-157.49
-0.6	1.11327	0.51	-62.34	-157.74
-0.65	1.11335	0.51	-62.54	-157.98
-0.7	1.11343	0.51	-62.75	-158.23
-0.75	1.11351	0.51	-62.96	-158.48
-0.8	1.11359	0.52	-63.17	-158.72
-0.85	1.11367	0.52	-63.37	-158.97
-0.9	1.11375	0.52	-63.58	-159.22
-0.95	1.11383	0.52	-63.79	-159.47
-1	1.11391	0.52	-64.00	-159.71
-1.05	1.11399	0.52	-64.21	-159.96
-1.1	1.11407	0.52	-64.42	-160.21
-1.15	1.11415	0.52	-64.63	-160.46
-1.2	1.11423	0.53	-64.84	-160.71
-1.25	1.11431	0.53	-65.05	-160.96
-1.3	1.11439	0.53	-65.26	-161.21
-1.35	1.11447	0.53	-65.47	-161.46
-1.4	1.11455	0.53	-65.69	-161.71
-1.45	1.11463	0.53	-65.90	-161.96
-1.5	1.11471	0.53	-66.11	-162.21
-1.55	1.11479	0.53	-66.32	-162.46
-1.6	1.11487	0.54	-66.54	-162.72
-1.65	1.11495	0.54	-66.75	-162.97
-1.7	1.11503	0.54	-66.96	-163.22
-1.75	1.11511	0.54	-67.18	-163.47
-1.8	1.11519	0.54	-67.39	-163.73
-1.85	1.11527	0.54	-67.61	-163.98
-1.9	1.11536	0.54	-67.82	-164.23
-1.95	1.11544	0.54	-68.04	-164.49
-2	1.11552	0.54	-68.25	-164.74
-2.05	1.11560	0.55	-68.47	-164.99

-2.1	1.11568	0.55	-68.69	-165.25
-2.15	1.11576	0.55	-68.90	-165.50
-2.2	1.11584	0.55	-69.12	-165.76
-2.25	1.11592	0.55	-69.34	-166.02
-2.3	1.11601	0.55	-69.55	-166.27
-2.35	1.11609	0.55	-69.77	-166.53
-2.4	1.11617	0.55	-69.99	-166.78
-2.45	1.11625	0.56	-70.21	-167.04
-2.5	1.11633	0.56	-70.43	-167.30
-2.55	1.11641	0.56	-70.65	-167.55
-2.6	1.11650	0.56	-70.87	-167.81
-2.65	1.11658	0.56	-71.09	-168.07
-2.7	1.11666	0.56	-71.31	-168.33
-2.75	1.11674	0.56	-71.53	-168.59
-2.8	1.11682	0.56	-71.75	-168.85
-2.85	1.11691	0.57	-71.97	-169.10
-2.9	1.11699	0.57	-72.19	-169.36
-2.95	1.11707	0.57	-72.41	-169.62
-3	1.11715	0.57	-72.63	-169.88
-3.05	1.11724	0.57	-72.86	-170.14
-3.1	1.11732	0.57	-73.08	-170.40
-3.15	1.11740	0.57	-73.30	-170.67
-3.2	1.11748	0.57	-73.52	-170.93
-3.25	1.11757	0.57	-73.75	-171.19
-3.3	1.11765	0.58	-73.97	-171.45
-3.35	1.11773	0.58	-74.20	-171.71
-3.4	1.11781	0.58	-74.42	-171.97
-3.45	1.11790	0.58	-74.65	-172.24
-3.5	1.11798	0.58	-74.87	-172.50
-3.55	1.11806	0.58	-75.10	-172.76
-3.6	1.11815	0.58	-75.32	-173.03
-3.65	1.11823	0.58	-75.55	-173.29
-3.7	1.11831	0.58	-75.78	-173.55
-3.75	1.11840	0.59	-76.00	-173.82
-3.8	1.11848	0.59	-76.23	-174.08
-3.85	1.11856	0.59	-76.46	-174.35
-3.9	1.11865	0.59	-76.68	-174.61
-3.95	1.11873	0.59	-76.91	-174.88
-4	1.11881	0.59	-77.14	-175.15
-4.05	1.11890	0.59	-77.37	-175.41
-4.1	1.11898	0.59	-77.60	-175.68
-4.15	1.11907	0.59	-77.83	-175.95
-4.2	1.11915	0.60	-78.06	-176.21
-4.25	1.11923	0.60	-78.29	-176.48
-4.3	1.11932	0.60	-78.52	-176.75
-4.35	1.11940	0.60	-78.75	-177.02
-4.4	1.11949	0.60	-78.98	-177.28
-4.45	1.11957	0.60	-79.21	-177.55
-4.5	1.11965	0.60	-79.44	-177.82
-4.55	1.11974	0.60	-79.68	-178.09
-4.6	1.11982	0.60	-79.91	-178.36
-4.65	1.11991	0.61	-80.14	-178.63
-4.7	1.11999	0.61	-80.38	-178.90
-4.75	1.12008	0.61	-80.61	-179.17
-4.8	1.12016	0.61	-80.84	-179.44
-4.85	1.12025	0.61	-81.08	-179.71
-4.9	1.12033	0.61	-81.31	-179.98
-4.95	1.12042	0.61	-81.55	-180.26
-5	1.12050	0.61	-81.78	-180.53